S.G. Jorstad, A.P. Marscher, C.M. Raiteri, M. Villata, Z.R. Weaver, H. Zhang, L. Dong, J.L. Gómez, M.V. Perel, S.S. Savchenko, V.M. Larionov, D. Carosati, W.P. Chen, O.M. Kurtanidze, A. Marchini, K. Matsumoto, F. Mortari, P. Aceti, J.A. Acosta-pulido, T. Andreeva, G. Apolonio, C. Arena, A. Arkharov, R. Bachev, M. Banfi, G. Bonnoli, G.A. Borman, V. Bozhilov, M.I. Carnerero, G. Damljanovic, S.A. Ehgamberdiev, D. Elsässer, A. Frasca, D. Gabellini, T.S. Grishina, A.C. Gupta, V.A. Hagen-thorn, M.K. Hallum, M. Hart, K. Hasuda, F. Hemrich, H.Y. Hsiao, S. Ibryamov, T.R. Irsmambetova, D.V. Ivanov, M.D. Joner, G.N. Kimeridze, S.A. Klimanov, J. Knött, E.N. Kopatskaya, S.O. Kurtanidze, A. Kurtenkov, T. Kuutma, E.G. Larionova, S. Leonini, H.C. Lin, C. Lorey, K. Mannheim, G. Marino, M. Minev, D.O. Mirzaqulov, D.A. Morozova, A.A. Nikiforova, M.G. Nikolashvili, E. Ovcharov, R. Papini, T. Pursimo, I. Rahimov, D. Reinhart, T. Sakamoto, F. Salvaggio, E. Semkov, D.N. Shakhovskoy, L.A. Sigua, R. Steineke, M. Stojanovic, A. Strigachev, Y.V. Troitskaya, I.S. Troitskiy, A. Tsai, A. Valcheva, A.A. Vasilyev, O. Vince, L. Waller, E. Zaharieva, R. Chatterjee

Rapid Quasi-Periodic Oscillations in the Relativistic Jet of BL Lacertae

Nature, Vol. 609, N. 7926, 2022, p. 265-268
doi:10.1038/s41586-022-05038-9

Article

Rapid quasi-periodic oscillations in the relativistic jet of BL Lacertae

https://doi.org/10.1038/s41586-022-05038-9

Received: 29 January 2022

Accepted: 28 June 2022

Published online: 7 September 2022

Check for updates

S. G. Jorstad[1,2]✉, A. P. Marscher[1], C. M. Raiteri[3], M. Villata[3], Z. R. Weaver[1], H. Zhang[4,5], L. Dong[6], J. L. Gómez[7], M. V. Perel[8], S. S. Savchenko[2,9,10], V. M. Larionov[2,10,47], D. Carosati[11,12], W. P. Chen[13], O. M. Kurtanidze[14,15,16], A. Marchini[17], K. Matsumoto[18], F. Mortari[19], P. Aceti[20,21], J. A. Acosta-Pulido[22], T. Andreeva[23], G. Apolonio[24], C. Arena[25], A. Arkharov[10], R. Bachev[26], M. Banfi[20], G. Bonnoli[7,17,27], G. A. Borman[28], V. Bozhilov[29], M. I. Carnerero[3], G. Damljanovic[30], S. A. Ehgamberdiev[31,32], D. Elsässer[33,34], A. Frasca[35], D. Gabellini[19], T. S. Grishina[2], A. C. Gupta[36], V. A. Hagen-Thorn[2], M. K. Hallum[1], M. Hart[1], K. Hasuda[37], F. Hemrich[33], H. Y. Hsiao[13], S. Ibryamov[38], T. R. Irsmambetova[39], D. V. Ivanov[23], M. D. Joner[24], G. N. Kimeridze[14], S. A. Klimanov[10], J. Knött[33], E. N. Kopatskaya[2], S. O. Kurtanidze[14,16], A. Kurtenkov[26], T. Kuutma[40], E. G. Larionova[2], S. Leonini[41], H. C. Lin[13], C. Lorey[33], K. Mannheim[33,42], G. Marino[25,43], M. Minev[29], D. O. Mirzaqulov[31], D. A. Morozova[2], A. A. Nikiforova[2,10], M. G. Nikolashvili[14,16], E. Ovcharov[29], R. Papini[43], T. Pursimo[44,45], I. Rahimov[23], D. Reinhart[33], T. Sakamoto[37], F. Salvaggio[25,43], E. Semkov[26], D. N. Shakhovskoy[28], L. A. Sigua[14], R. Steineke[33], M. Stojanovic[30], A. Strigachev[26], Y. V. Troitskaya[2], I. S. Troitskiy[2], A. Tsai[13], A. Valcheva[29], A. A. Vasilyev[2], O. Vince[30], L. Waller[33], E. Zaharieva[29] & R. Chatterjee[46]

Blazars are active galactic nuclei (AGN) with relativistic jets whose non-thermal radiation is extremely variable on various timescales[1–3]. This variability seems mostly random, although some quasi-periodic oscillations (QPOs), implying systematic processes, have been reported in blazars and other AGN. QPOs with timescales of days or hours are especially rare[4] in AGN and their nature is highly debated, explained by emitting plasma moving helically inside the jet[5], plasma instabilities[6,7] or orbital motion in an accretion disc[7,8]. Here we report results of intense optical and γ-ray flux monitoring of BL Lacertae (BL Lac) during a dramatic outburst in 2020 (ref. [9]). BL Lac, the prototype of a subclass of blazars[10], is powered by a 1.7×10^8 M_{Sun} (ref. [11]) black hole in an elliptical galaxy (distance = 313 megaparsecs (ref. [12])). Our observations show QPOs of optical flux and linear polarization, and γ-ray flux, with cycles as short as approximately 13 h during the highest state of the outburst. The QPO properties match the expectations of current-driven kink instabilities[6] near a recollimation shock about 5 parsecs (pc) from the black hole in the wake of an apparent superluminal feature moving down the jet. Such a kink is apparent in a microwave Very Long Baseline Array (VLBA) image.

In 2020, the Whole Earth Blazar Telescope (WEBT; https://www.oato.inaf.it/blazars/webt/) observed the highest-amplitude optical outburst of BL Lac (redshift $z = 0.069$ (ref. [13])) in 20 years (ref. [9]), acquiring 16,497 flux-density measurements from 1 March 2020 to 31 December 2020 (modified Julian date (MJD) 58,909–59,215) in the optical Cousins R-band ($\lambda_{eff} = 635$ nm), using 37 telescopes (Extended Data Table 1). Five telescopes also conducted 1,285 R-band measurements of the degree, P_R, and position angle, χ_R, of linear polarization. Figure 1a plots the R-band light curve (Methods). The dense sampling leads to the discovery of QPOs in flux, S_R, with a duration <1 day. Figure 1b shows 14 pulses detected over a 2-week interval during the highest-flux state. The outburst began around 20 July (MJD 59,050) and then peaked on 21 August (MJD 59,082.98608) and again on 5 October (MJD 59,127.68480) at R-magnitude of about 11.9, with a high-flux plateau between the peaks (Fig. 1a); it ended by 17 October (MJD 59,140). During the plateau, P_R (Extended Data Fig. 1b) underwent intraday, high-amplitude oscillations, from <1% to 20%, whereas χ_R rotated by approximately 200° over 0.3 days near the beginning of the outburst (when P_R was low, implying turbulence) and then varied on day timescales. We find no statistically significant correlation between S_R and P_R, which suggests strong turbulence superposed on the kink instability (Methods). The variations of χ_R form arc-like structures in Fig. 2 on timescales ≤1 day. The high degree of polarization and similarity of the S_R and P_R QPO timescales imply that the QPOs occur in the jet rather than the accretion disc, as commonly inferred in X-ray binary systems[14] and Seyfert galaxies[15]. BL Lac is a bright γ-ray source[16,17] and Extended Data Fig. 1 presents the 0.1–300-GeV γ-ray light curve during the outburst constructed using the Fermi Large Area Telescope data (Methods). There is a strong correlation (coefficient $\rho = 0.62 \pm 0.04$) between the optical and γ-ray light curves, with no statistically significant delay ($-0.02^{+0.05}_{-0.44}$ days; Extended

A list of affiliations appears at the end of the paper.

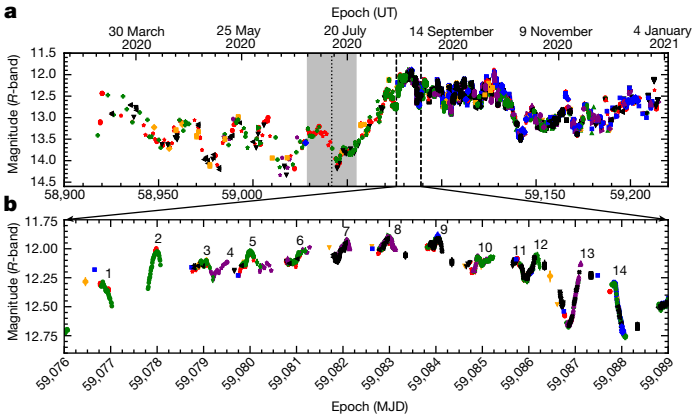

Fig. 1 | Optical *R*-band light curves. a, For the whole period of monitoring from 1 March 2020 to 31 December 2020 (n = 16,497). The grey area denotes the time of ejection of superluminal knot K and its 1σ uncertainty. **b**, At the high state of the outburst from 15 to 28 August (n = 2,145). Different symbols and colours in both panels indicate observations conducted by different telescopes, designations of which are given in Extended Data Table 1. The error bars represent 1σ uncertainties, which are, in general, less than the symbol sizes.

Data Fig. 2); this implies co-spatiality of the optical and γ-ray emission regions.

We have imaged BL Lac in total and polarized intensity monthly at 43 GHz with the VLBA at a resolution of about 0.1 milliarcseconds (mas)[18] or 0.13 pc. The images (Fig. 3a, Extended Data Fig. 3 and Methods) feature a jet extending southward from a bright 'core' (A0, presumed stationary). Modelling of the images[19] shows quasi-stationary components A1–A3 located 0.12 ± 0.03, 0.29 ± 0.05 and 0.38 ± 0.09 mas from A0, respectively. We interpret these features, which have persisted for >15 years (refs. [20,21]), as a series of recollimation shocks resulting from pressure mismatches between the jet and its surroundings[22,23]. We also identify (Fig. 3b) a bright knot, K, moving at 3.32 ± 0.46 mas year^{-1} (apparent speed β_{app} = 15.2 ± 2.1c), which passed through A0 on 11 July 2020 (MJD 59,042 ± 13), when the outburst began (Fig. 1). The mean travel time of K from one stationary feature to another is about 14 days. According to previous observations since 1998 (refs. [19,21,24]), the jet usually moves with a Lorentz factor Γ of about 6 and viewing angle Θ_o of about 5° (refs. [21,24]); β_{app} of approximately 15c (the highest yet observed[24]) requires that the jet accelerated to at least Γ of about 15 in mid-2020 and changed its direction to Θ_o around $1/\Gamma$ corresponding to 3.8°. The Doppler factor $\delta = (\Gamma(1 - \beta\cos\Theta_o))^{-1}$ then increased from 9 to 15 after K crossed the core at the onset of the outburst. K passed through stationary feature A2 on MJD 59,075 ± 10 (Fig. 3b) during the first peak of the outburst and the start of QPOs (Fig. 2). If the distance of A0 from the vertex of the jet is around 0.5 pc (ref. [25]), A2 is located about 5 pc (deprojected) from the black hole, where Cohen et al.[26] determined that the plasma pressure is dominated by a helical magnetic field, a condition favourable for the development of current-driven kink instabilities in a jet[6]. Indeed, a kink is visible south-west of A2 during the outburst in Fig. 3a, which also indicates

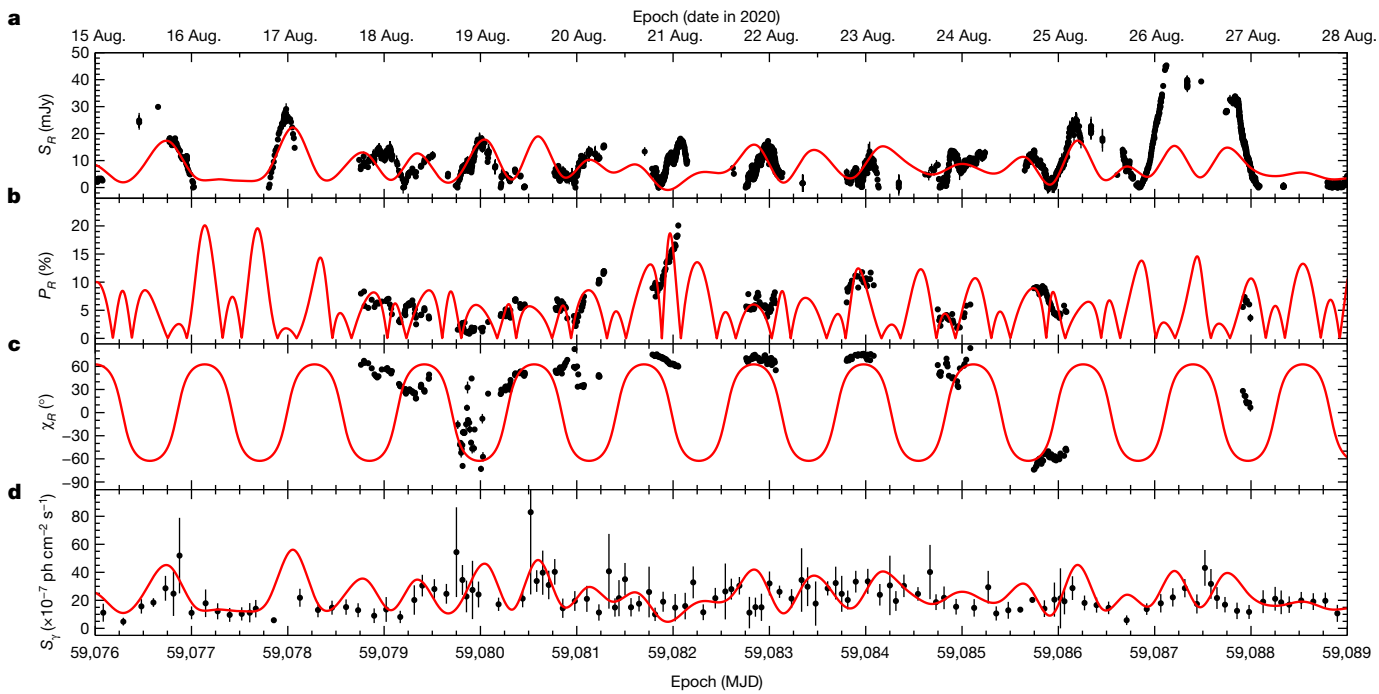

Fig. 2 | Model-data comparison. a, Optical flux densities in *R*-band (after removal of long-term trend, n = 2,145). **b**, Degree of polarization (n = 309). **c**, position angle of polarization (n = 309). **d**, γ-Ray light curve during the high state of the outburst (n = 128). Black symbols correspond to the data (error bars represent 1σ uncertainties) and solid red curves show fitting of a kink instability model to the data using an MCMC code (see text). ph, photons.

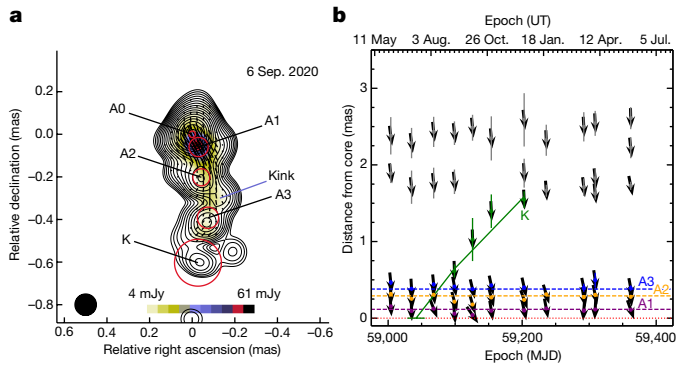

Fig. 3 | Parsec-scale jet of BL Lac. a, VLBA total (contours) and polarized (colour scale) intensity image of BL Lac at 43 GHz on 7 September 2020, convolved with a circular beam of radius 0.1 mas at PA = 0° (bottom-left circle). The global intensity peak is 1.944 Jy beam^{-1} and contour levels start at 0.35% of the peak and increase by factors of √2. The red circles represent the FWHM of Gaussian components according to models of the flux intensity distribution. Black line segments in the image show the electric vector (polarization) direction. **b**, Distance of knots with respect to the core (dotted red line) versus time, with each vector indicating knot position angle at a given time (error bars correspond to 1σ uncertainties). The dashed lines show the average locations of stationary features A1, A2 and A3, and the solid green line approximates the motion of superluminal knot K.

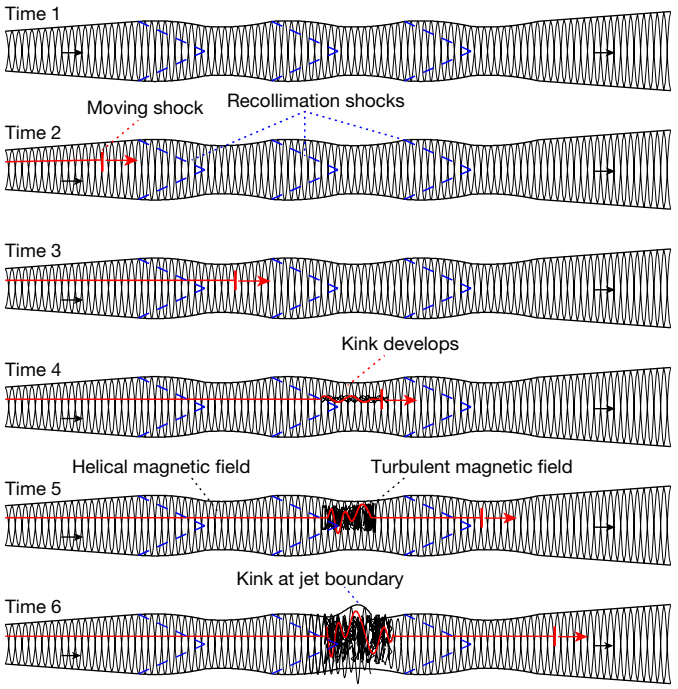

Fig. 4 | Sketch of the development of the QPOs. Jet flow is from left to right (corresponding to north-to-south in BL Lac). Interaction of an off-axis moving shock with a standing recollimation shock triggers a kink instability, which grows, causes quasi-periodic structure to form, leading to QPO emission and disrupts the magnetic field, whose structure changes from helical to turbulent. The peak of the outburst occurs during times 5 and 6.

that the position angle of polarization at 43 GHz is along the jet, as expected for a tight helical field.

Visual inspection of Figs. 1b and 2 clearly identifies pulses that repeat on a timescale <1 day. We have used different methods of time series analysis—REDFIT[27] periodogram, continuous wavelet transform (CWT)[28] and weighted wavelet Z-transform (WWZ)[29] (Methods)—to search for periodicity in the optical and γ-ray flux and P_R data. The periodograms (Extended Data Fig. 4) indicate QPOs of around 0.5–0.55 days for all three datasets with ≥99% significance. Both wavelet methods show that the periodicity is transient (Extended Data Figs. 5 and 6). A QPO of 0.55 days is detected during MJD 59,076–59,112 at 99% significance in *R*-band (CWT, WWZ) and γ-ray (CWT) fluxes, and P_R (WWZ). The CWT P_R scalogram also possesses the most significant period, about 0.55 days, during the same time interval, but with 92% significance. There are other periods ≤1 day apparent at 99% significance, but they do not agree among the methods and different arrays. We have applied a trial-period method for the *R*-band measurements over MJD 59,076–59,112 using a sinusoidal function, finding that a period of 0.55 days yields the lowest χ^2 value (Extended Data Fig. 7a and Methods). Therefore, the period of 0.55 days is the most consistent among the methods and datasets. Comparison of the average S_R and P_R pulses indicates that, although the average P_R pulse has a wider profile than that of S_R (Extended Data Fig. 7b,c and Methods), they are clearly similar, implying that the S_R and P_R oscillations are produced by means of the same process. In addition, the wavelet methods show QPOs of 4–5 days with 99% significance identified in the middle of the outburst (MJD 59,100–59,130) and a period of approximately 14–15 days, with similar significance during the first half of the outburst.

We attribute the 0.55-day QPOs to a current-driven kink instability, triggered when the jet is perturbed by a lateral displacement[6]. This random process occurred near stationary feature A2, associated with a recollimation shock where Alfvén waves are excited[26]. Growth of the kink creates two further effects: (1) development of contiguous regions in which magnetic field lines become oppositely directed, then reconnect to accelerate electrons, which produce electromagnetic radiation whose flux and polarization oscillate; and (2) driving of turbulence that disorders the magnetic field and accelerates electrons that generate radiation with very low polarization and random fluctuations.

The multiwavelength outburst results from a combination of the increase in flow Lorentz factor, which sends a shock wave down the jet (knot K), a decrease in viewing angle, a kink in the jet and its magnetic field, and turbulence. The size of a kink grows with time[30], which could explain the approximately 4-day QPOs in the second half of the outburst, whereas the QPO of about 14 days during the first half can arise from the passage of K through successive stationary features A0–A3 (see above).

We model the polarized optical flux as synchrotron radiation and the γ-ray flux as synchrotron self-Compton emission, using jet parameters derived from the VLBA data, Γ of about 15, Θ_o of about 3.8° and δ of about 15. The model assumes that the magnetic field is a superposition of constant toroidal, periodically fluctuating poloidal and turbulent components (Methods). We use Markov chain Monte Carlo (MCMC) fitting to constrain the toroidal and poloidal components, the fluctuation amplitudes of the optical and γ-ray flux, the quasi-period and the average turbulent contribution (Extended Data Fig. 8a). We find that the full period of the twist in the kink of about 1.1 days (involving only the poloidal component) corresponds to the period in χ_R, whereas the flux and P_R have a period of half this value, 0.55 days (Extended Data Fig. 8a), which coincides with the result of the time series analyses. The QPO expected from a kink has an observed period of about $\frac{\Delta r(1+z)}{2v_\perp \delta}$, in which Δr is the size of the kink and $v_\perp$ is the transverse velocity, estimated at about 0.1–0.2c (ref. [6]). This yields Δr of around 8×10^{15} cm (roughly 3 light-days), which is similar to the theoretical expectation, Δr approximately 10^{16} cm (ref. [6]). Figure 2 compares S_R, P_R, χ_R and γ-ray flux versus time with the MCMC fit. Figure 4 sketches the development of the kink instability as a superluminal disturbance propagates through recollimation shocks, a scenario that results in short-timescale QPOs.

Online content

Any methods, additional references, Nature Research reporting summaries, source data, extended data, supplementary information,

acknowledgements, peer review information; details of author contributions and competing interests; and statements of data and code availability are available at https://doi.org/10.1038/s41586-022-05038-9.

1. Raiteri, C. M. et al. Blazar spectral variability as explained by a twisted inhomogeneous jet. *Nature* **552**, 374–377 (2017).
2. Wehrle, A. E. et al. Erratic flaring of BL Lac in 2012–2013: multiwavelength observations. *Astrophys. J.* **816**, 53 (2016).
3. Larionov, V. M. et al. Multiwavelength behaviour of the blazar 3C 279: decade-long study from γ-ray to radio. *Mon. Not. R. Astron. Soc.* **492**, 3829–3848 (2020).
4. Gupta, A. Multi-wavelength intra-day variability and quasi-periodic oscillation in blazars. *Galaxies* **6**, 1 (2018).
5. Sarkar, A. et al. Multi-waveband quasi-periodic oscillations in the light curves of blazar CTA 102 during its 2016–2017 optical outburst. *Astron. Astrophys.* **642**, 129–137 (2020).
6. Dong, L., Zhang, H. & Giannios, D. Kink instabilities in relativistic jets can drive quasi-periodic radiation signatures. *Mon. Not. R. Astron. Soc.* **494**, 1817–1825 (2020).
7. Roy, A. et al. Transient quasi-periodic oscillations at γ-rays in the TeV blazar PKS 1510-089. *Mon. Not. R. Astron. Soc.* **510**, 3641–3649 (2021).
8. Hong, S., Xiong, D. & Bai, J. Optical quasi-periodic oscillation of the BL Lacertae object S5 0716+714 during the faint state. *Astron. J.* **155**, 31 (2018).
9. Grishina, T. S. & Larionov, V. M. The blazar BL Lac reaches historical maximum. The Astronomer's Telegram, no. 13930 (2020).
10. Stickel, M. et al. The complete sample of 1 Jansky BL Lacertae objects. I - Summary properties. *Astrophys. J.* **374**, 431–439 (1991).
11. Woo, J.-H. & Urry, C. M. Active galactic nucleus black hole masses and bolometric luminosities. *Astrophys. J.* **579**, 530 (2002).
12. Bennett, C. L. et al. The 1% concordance Hubble constant. *Astrophys. J.* **794**, 135 (2014).
13. Miller, J. S., French, H. B. & Hawley, S. A. The spectrum and magnitude of the galaxy associated with BL Lacertae. *Astrophys. J.* **219**, L85–L87 (1978).
14. Remillard, R. A. & McClintock, J. E. X-ray properties of black-hole binaries. *Annu. Rev. Astron. Astrophys.* **44**, 49–92 (2006).
15. Ashton, D. I. & Middleton, M. J. Searching for energy-resolved quasi-periodic oscillation in AGN. *Mon. Not. R. Astron. Soc.* **501**, 5478–5499 (2021).
16. Abdollahi, S. et al. Fermi large area telescope fourth source catalog. *Astrophys. J. Suppl. Ser.* **247**, 33 (2020).
17. Albert, J. et al. Discovery of very high energy γ-ray emission from the low-frequency-peaked BL Lacertae object BL Lacertae. *Astrophys. J.* **666**, L17 (2007).
18. *BEAM-ME program – Blazars Entering the Astrophysical Multi-Messenger Era* http://www.bu.edu/blazars/BEAM-ME.html (2022).
19. Jorstad, S. G. et al. Polarimetric observations of 15 active galactic nuclei at high frequencies: jet kinematics from bimonthly monitoring with the Very Long Baseline Array. *Astron. J.* **130**, 1418–1466 (2005).
20. Cohen, M. H. et al. Studies of the jet in BL Lacertae. I. Recollimation shock and moving emission features. *Astrophys. J.* **787**, 151–160 (2014).
21. Jorstad, S. G. et al. Kinematics of parsec-scale jets of gamma-ray blazars at 43 GHz within the VLBA-BU-BLAZAR program. *Astrophys. J.* **846**, 98–132 (2017).
22. Gómez, J. L. et al. Hydrodynamical models of superluminal sources. *Astrophys. J.* **482**, L33 (1997).
23. Fuentes, A., Gómez, J. L., Martí, J. M. & Perucho, M. Total and linearly polarized synchrotron emission from overpressured magnetized relativistic jets. *Astrophys. J.* **860**, 121 (2018).
24. Lister, M. L. et al. Monitoring of jets in active galactic nuclei with VLBA experiments. XVIII. Kinematics and inner jet evolution of bright radio-loud active galaxies. *Astrophys. J.* **923**, 30 (2021).
25. O'Sullivan, S. P. & Gabuzda, D. C. Magnetic field strength and spectral distribution of six parsec-scale active galactic nuclei jets. *Mon. Not. R. Astron. Soc.* **400**, 26–42 (2009).
26. Cohen, M. H. et al. Studies of the Jet in BL Lacertae. II. Superluminal Alfvén waves. *Astrophys. J.* **803**, 3 (2015).
27. Schulz, M. & Mudelsee, M. REDFIT: estimating red-noise spectra directly from unevenly spaced paleoclimatic time series. *Comput. Geosci.* **28**, 421–426 (2002).
28. Grossman, A., Kronland-Martinet & R. Morlet, J. in *Wavelets: Time-Frequency Methods and Phase Space* (eds Combes, J.-M., Grossman, A. & Tchamitchinan, P.) 2–20 (Springer, 1989).
29. Foster, G. Wavelets for period analysis of unevenly sampled time series. *Astron. J.* **112**, 1709–1729 (1996).
30. Barniol, D. R., Tchekhovskoy, A. & Giannios, D. Simulations of AGN jets: magnetic kink instability versus conical shocks. *Mon. Not. R. Astron. Soc.* **469**, 4957–4978 (2017).

[1]Institute for Astrophysical Research, Boston University, Boston, MA, USA. [2]Astronomical Institute, St. Petersburg State University, St. Petersburg, Russia. [3]INAF, Osservatorio Astrofisico di Torino, Torino, Italy. [4]NASA Postdoctoral Program Fellow, Greenbelt, MD, USA. [5]NASA Goddard Space Flight Center, Greenbelt, MD, USA. [6]Department of Physics, Purdue University, West Lafayette, IN, USA. [7]Instituto de Astrofísica de Andalucía (CSIC), Granada, Spain. [8]St. Petersburg State University, St. Petersburg, Russia. [9]Special Astrophysical Observatory, Russian Academy of Sciences, Nizhnii Arkhyz, Russia. [10]Pulkovo Observatory, St. Petersburg, Russia. [11]EPT Observatories, Tijarafe, La Palma, Spain. [12]INAF, TNG Fundación Galileo Galilei, La Palma, Spain. [13]Graduate Institute of Astronomy, National Central University, Taoyuan, Taiwan. [14]Abastumani Observatory, Mt. Kanobili, Abastumani, Georgia. [15]Engelhardt Astronomical Observatory, Kazan Federal University, Tatarstan, Russia. [16]Zentrum für Astronomie der Universität Heidelberg, Landessternwarte, Heidelberg, Germany. [17]Astronomical Observatory, Department of Physical Sciences, Earth and Environment, University of Siena, Siena, Italy. [18]Astronomical Institute, Osaka Kyoiku University, Kashiwara, Japan. [19]Hypatia Observatory, Rimini, Italy. [20]Osservatorio Astronomico Città di Seveso, Seveso, Italy. [21]Department of Aerospace Science and Technology, Politecnico di Milano, Milano, Italy. [22]Instituto de Astrofísica de Canarias and Dpto. de Astrofísica, Universidad de La Laguna, Tenerife, Spain. [23]Institute of Applied Astronomy, Russian Academy of Sciences, St. Petersburg, Russia. [24]Department of Physics and Astronomy, Brigham Young University, Provo, UT, USA. [25]Gruppo Astrofili Catanesi (GAC), Catania, Italy. [26]Institute of Astronomy and National Astronomical Observatory, Bulgarian Academy of Sciences, Sofia, Bulgaria. [27]INAF-Osservatorio Astronomico di Brera, Merate, Italy. [28]Crimean Astrophysical Observatory RAS, Bakhchisaray, Crimea. [29]Department of Astronomy, Faculty of Physics, University of Sofia, Sofia, Bulgaria. [30]Astronomical Observatory Belgrade, Belgrade, Serbia. [31]Ulugh Beg Astronomical Institute, Tashkent, Uzbekistan. [32]National University of Uzbekistan, Tashkent, Uzbekistan. [33]Hans-Haffner-Sternwarte, Naturwissenschaftliches Labor für Schüler am FKG, Würzburg, Germany. [34]Department of Physics, TU Dortmund University, Dortmund, Germany. [35]INAF-Osservatorio Astrofisico di Catania, Catania, Italy. [36]Aryabhatta Research Institute of Observational Sciences (ARIES), Nainital, India. [37]Department of Physical Sciences, Aoyama Gakuin University, Tokyo, Japan. [38]Department of Physics and Astronomy, Faculty of Natural Sciences, University of Shumen, Shumen, Bulgaria. [39]Sternberg Astronomical Institute, M.V. Lomonosov Moscow State University, Moscow, Russia. [40]Centro de Estudios de Física del Cosmos de Aragón, Teruel, Spain. [41]Montarrenti Observatory, Siena, Italy. [42]Lehrstuhl für Astronomie, Universität Würzburg, Würzburg, Germany. [43]Wild Boar Remote Observatory, Florence, Italy. [44]Nordic Optical Telescope, Santa Cruz de Tenerife, Spain. [45]Department of Physics and Astronomy, Aarhus University, Aarhus C, Denmark. [46]Department of Physics, Presidency University, Kolkata, India. [47]Deceased: V. M. Larionov. ✉e-mail: jorstad@bu.edu

Methods

Optical *R*-band photometric and polarimetric data reduction

Extended Data Table 1 presents the telescopes that participated in the campaign, along with the number of observations and designations used in Fig. 1 and Extended Data Fig. 1, and an average 1σ uncertainty of measurements provided by each telescope. Optical photometric data reduction and the *R*-band light curve compilation were performed following prescriptions described in detail in Villata et al.[31] Out of 37 telescopes indicated in Extended Data Table 1, 23 have participated in many BL Lac WEBT campaigns, for example, refs. [31–33], and their photometric systems (BVRI) are very well aligned on the basis of comparison stars used for BL Lac (B, C and H)[34]. We have analysed whether measurements from each telescope show a constant shift (exceeding an average 1σ uncertainty) with respect to telescopes that are consistent with each other for observations simultaneous within 15–30 min. If so, we have corrected all measurements from this telescope according to the shift. Applied shifts range from 0.02 to 0.26 magnitude. For two telescopes that provided measurements with a 1σ uncertainty > 0.075 magnitude, we have performed weighted averaging of individual measurements over 10–15 min (observations were performed every 3–5 min) and used the corresponding standard deviation as the uncertainty. Of the 16,659 observations originally submitted, 0.2% were removed from the dataset based on a significant (>3σ) deviation from the general behaviour at a given time. We consider that our *R*-band light curve is very robust. The dataset was corrected for Galactic extinction and host-galaxy contamination, and transformed into flux density units following the technique described in Weaver et al.[33]. The polarization observations from different telescopes were aligned using standard polarized stars (VI Cyg #12, Hiltner 960, BD+64.106 and BD+59.389) from Schmidt et al.[35] observed during the campaign. Data were corrected for instrumental and interstellar polarization using comparison stars B, C and H, and the contribution of unpolarized host-galaxy starlight was taken into account in the same manner as in Weaver et al.[33]. Extended Data Fig. 1 shows the *R*-band flux density and polarization parameters P_R and χ_R versus time from 1 March 2020 to 31 December 2020, after applying all corrections.

γ-Ray data reduction

We have downloaded photon and spacecraft data of the Fermi Large Area Telescope provided by the Fermi Space Science Center. The γ-ray data were analysed using the FermiTools package version 2.0.8 installed with Conda (https://github.com/fermi-lat/Fermitools-conda/), with instrument response function P8R2_V6, Galactic diffuse emission model gll_iem_v06, and isotropic background model iso_P8R2_SOURCE_V6_v06. To build a γ-ray light curve, we applied an unbinned likelihood analysis in the 0.1–300-GeV energy range. The background model includes all sources from the 4FGL catalogue[16] inside a 15° radius surrounding BL Lac. Fluxes of the sources within a 10° radius were set as free parameters of the model, whereas fluxes of more distant sources were fixed to their mean values according to the 4FGL catalogue. The flux of BL Lac itself was modelled using a log-parabolic spectral energy distribution with spectral parameters fixed to their catalogue values (α_g = 2.14, β_g = 0.06 and E_b = 796.15 MeV). To obtain the highest possible temporal resolution of the γ-ray light curve, we used an adaptive temporal binning strategy. We started the integration with a 1-h bin and increased it gradually by increments of 1 h until we reached a likelihood test statistic value TS ≥ 10 (which corresponds to an approximately 3σ detection level)[36]. This strategy allows one to attain the highest possible temporal resolution during active periods while still obtaining a robust signal level during quiescent states. Extended Data Fig. 1d shows the γ-ray light curve for the 2020 analysed time intervals, whereas Fig. 2d plots the γ-ray light curve during the peak of the outburst.

Correlation analysis

We used the *z*-transformed discrete correlation function[37], with uncertainties derived by sampling errors based on the noise in the original data and calculated with 100 random Monte Carlo draws. To compute 1σ-like bounds on the derived time lag, we used the 'peak likelihood' algorithm (PLIKE)[38], which estimates the probability of a correlation without any a priori knowledge about the shape of the correlation function or flux/polarization curves. To verify the significance of the correlations (or non-correlations), we used a bootstrap method of generating 3,000 pairs of artificial flux and polarization curves of the same duration and temporal cadence, using the algorithm suggested by Emmanoulopoulos et al.[39], in which the power spectral density (PSD) and probability density function (PDF) of each curve correspond to those of the observed data. Specifically, the *R*-band flux and polarization PDFs were modelled by normal distributions, whereas the γ-ray PDF was modelled by a log-normal distribution (with means and standard deviations derived from the data in each case). The PSDs of the data were calculated using the power spectral response method[40–42]. We attempted to fit the PSD with a simple power-law model having a negative slope and obtained a satisfactory fit for each curve. Further attempts to fit with a bending power-law model did not notably improve the success fraction. During the fitting, we varied the slope from −0.5 to −2.5 in steps of 0.05 and determined the best-fit value of the slope and its uncertainty from the range of success fractions obtained in the above iterations. This resulted in slopes of −1.7 ± 0.3, −1.5 ± 0.3 and −0.9 ± 0.3 for optical and γ-ray light curves and fractional polarization, respectively. These artificial curves have been used throughout the paper to estimate significances of our time series analyses. Extended Data Fig. 2 presents results of the correlation analysis between the *R*-band and γ-ray flux, and between S_R and P_R for the entire period shown in Extended Data Fig. 1, between *R*-band residuals (after subtraction of a long-term trend; see Extended Data Fig. 1a) and γ-ray flux, between *R*-band residuals and P_R, and between corresponding theoretical values of S_R and S_γ, and S_R and P_R, shown in Fig. 2.

Imaging with the Very Long Baseline Array

BL Lac is one of 35 AGN observed in the BEAM-ME programme[18] with the VLBA at 43 GHz, with roughly monthly cadence. The results presented here are based on 11 epochs of observations from June 2020 to May 2021. BL Lac was monitored with 12 scans of 4–6 min each, interspersed between observations of other sources from the sample, which provided the u-v spatial-frequency coverage needed to make images with a dynamic range of roughly 500:1. The data were calibrated and imaged following the same procedure as described in ref. [21], which uses the Astronomical Image Processing System (AIPS; provided by the National Radio Astronomy Observatory (NRAO)) and Difmap[43] software packages. The images were modelled in Difmap by circular components with Gaussian brightness distributions. Moving knot K was detected at four epochs at a distance between 0.5 and 1.5 mas from the core (Extended Data Fig. 3). Usually, this region has very low intensity at 43 GHz (ref. [44]), hence it is rare to detect such a feature there. The average flux density of the knot was about 100 mJy, with mean 1σ uncertainty of 13 mJy, which corresponds to detection of the feature at an approximately 8σ level.

Search for periodicity

We have performed a search for periodicity in the *R*-band and γ-ray flux and fractional polarization using the REDFIT method[27], which is specifically designed for unevenly spaced time series affected by red noise. REDFIT fits the red-noise spectrum with a first-order autoregressive process and compares it with that calculated as the mean of a number of Monte Carlo simulations. The ratio between the simulated red-noise spectrum and the theoretical spectrum is then used to correct the Lomb–Scargle Fourier transform[45] of the time series for the bias

owing to the sampling. Extended Data Fig. 4a–c shows the results of the application of the REDFIT technique to the optical flux densities and γ-ray flux and optical degree of polarization of BL Lac, respectively.

We have used a magnitude scalogram, which is the CWT[28] of a signal plotted in time–frequency space. A scalogram allows better time localization of high-frequency events, and better frequency localization of long-duration events, than traditional methods. We used the scalogram realization in MATLAB Wavelet Toolbox v.2021b using a Morlet wavelet with $\omega_o = 6$. Scalograms of the *R*-band and γ-ray flux and P_R versus time are shown in Extended Data Fig. 5a–c, respectively. We used the wavelet-based software for MATLAB developed by Torrence and Compo[46] (available at http://paos.colorado.edu/research/wavelets) along with artificial light curves (mentioned above) to analyse the significance of the periods seen in the scalograms, based on a standard χ^2 test.

As well as the above methods to search for periodicity, we have used the WWZ[29] to alleviate problems induced by large fluctuations of the local number density and edge effects[47]. We have used the publicly available Python script (https://github.com/skiehl/wwz) developed by O'Neill et al.[48]. We performed the WWZ using 150 frequency bins from 0.3 to 100 μHz, logarithmically spaced. We find that the recommended window decay rate of $c = (8/\pi^2)^{-1}$ is sufficient for our purposes[29,46]. Extended Data Fig. 6a–c shows the results of the WWZ for the *R*-band, γ-ray and fractional polarization data, respectively. To determine the significance of the peaks in the WWZ, we have used the 3,000 artificial curves generated for the correlation analysis and the estimate_significance subroutine of the WWZ script.

We have determined a long-term trend of the *R*-band light curve by constructing a spline drawn through the lowest points at intervals of around 0.5–1 days during the outburst. The spline is shown in Extended Data Fig. 1a. To analyse pulses, we subtracted the long-term trend from the *R*-band flux densities during the outburst; Extended Data Fig. 7a plots the residuals during MJD 59,076–59,112. We combined pulses 2, 5, 7, 8, 9 and 12, which have well-observed maxima (see Fig. 1b), and determined their average shape (Extended Data Fig. 7b), which is characterized by an asymmetric profile with amplitude 17 ± 4 mJy and full width at half maximum (FWHM) of about 7 h. We performed a similar analysis of pulses of the fractional polarization, combining them after normalizing each pulse relative to its maximum (Extended Data Fig. 7c), using all P_R pulses plotted in Fig. 2. The average P_R pulse has a similar shape as the average S_R pulse with FWHM of about 9 h. We have approximated the *R*-band behaviour during MJD 59,076–59,112 by fitting the oscillations with a sinusoidal function with different trial periods running from 0.35 to 1.65 days, with a step of 0.05 days, and trial amplitudes from 14 to 21 mJy, with a step of 1 mJy. Extended Data Fig. 7a presents the best (lowest reduced χ^2) sinusoidal approximation (solid red curve) of the observed oscillations, with a 0.55-day period and a 20-mJy amplitude. This supports the presence of a 0.55-day QPO during the outburst found by the time series analyses.

Kink instability model

We model the QPO patterns in the optical band with synchrotron emission from a kink in the jet and the γ-rays generated by Compton scattering of the synchrotron photons. Magnetohydrodynamic simulations[30,49] have shown that kink instabilities can naturally develop in a jet with a strong toroidal magnetic field. The distorted field lines in the kinks give rise to magnetic reconnection, accelerating particles and further disordering the field. Both the poloidal field component and the number of accelerated particles increase in the same location[50,51], which maintains the outburst of non-thermal radiation instigated by the moving shock crossing recollimation shock A2 (see Fig. 3a). The kink in the jet naturally becomes quasi-periodic, consisting of twisted magnetic field structures, referred to as kink nodes. The process results in a moving region (plasma 'blob') of enhanced emission, containing a few kink nodes[6,30], which trails the moving shock. Owing to the quasi-periodic nature of the kink, this blob can exhibit QPO radiation patterns as long as there are no more than a few nodes[52]. If the kink is strong with a small number of nodes, its transverse displacement is roughly equal to the size of the emission blob, which is what we find in BL Lac.

We have carried out semianalytical numerical simulations of time-dependent emission from such a blob with a kink following the formalism of Dong et al.[6]. There are three contributions: a constant toroidal component, whose flux is normalized to unity in the code, a periodically fluctuating poloidal contribution characterized by a sinusoidal function with period *T* and amplitude B_{p0}, and turbulence, whose contribution averages to P_0, with an amplitude of fluctuations of B_0. The optical and γ-ray light curves follow the same temporal evolution. The average emission power in the code unit is normalized to F_{o0} and $F_{\gamma 0}$ for the optical and γ-ray bands, respectively. We use MCMC fitting to constrain the above six parameters based on all-optical and γ-ray data during the interval MJD 59,076–59,089, totalling more than 3,000 data points. All six parameters converge well into a small parameter range using 64 MCMC walkers with 60,000 iterations (Extended Data Fig. 8a), which implies that our model is robust.

Figure 2 presents the model, calculated with the 50% quantile (median) of the fitted values of each parameter ($F_{o0} = 21.05$ mJy, $F_{\gamma 0} = 9.48 \times 10^{-7}$ photons cm^{-2} s^{-1} and $T = 1.14$ days, in the frame of the observer, and $B_{p0} = 1.93$, $B_0 = 2.80$ and $P_0 = 14.6$ are in scalable code units, measured in the comoving plasma frame). Note that we fit the main characteristics of the observed variations rather than the actual details, which would take many more simulations to reproduce owing to the random nature of the turbulence. The turbulent contribution affects both S_R (by addition) and P_R (by dilution), but not χ_R. To constrain the time profile, we use all simultaneous optical and polarization measurements (about 600 data points) to constrain the strength of the turbulent contribution through the least-squares method. The result is consistent with a Gaussian distribution. Therefore, we characterize the turbulent contribution at different times by a random number drawn from a Gaussian distribution centred at P_0, which is a new addition to the formalism of Dong et al.[6]. In the non-turbulent case considered in Dong et al.[6], there is a strong anti-correlation between S_R and P_R ($\rho \approx -1$). When turbulence is added to the code, the anti-correlation becomes statistically insignificant, in agreement with the observations (Extended Data Fig. 2). The model light curves show a positive correlation between optical flux densities and γ-ray fluxes without a delay, as the BL Lac data do. Magnetohydrodynamic simulations have shown that both the toroidal and the poloidal magnetic field components, as well as the non-thermal particle distributions, can exhibit considerable randomness[48–50], which can contribute to the random behaviour in the evolution of χ_R. For the sake of simplicity, we do not include randomness in the toroidal and poloidal field components in our effort to capture the main physical characteristics of the variations. Extended Data Fig. 8b–e plots distributions of residuals between the data and the model for all four observables. The histograms have shapes close to a Gaussian distribution, with peaks near zero, as expected if the model represents the observed behaviour. The strength of our result comes from the extraordinary sampling, the number of QPO pulses and from the comprehensive interpretation of the multiwavelength behaviour, including polarization and VLBA images, which seem to be necessary components for understanding short-timescale QPOs in black-hole systems with relativistic jets.

Data availability

The data taken and assembled by the WEBT collaboration are stored in the WEBT archive at the Osservatorio Astrofisico di Torino, INAF (https://www.oato.inaf.it/blazars/webt/). The published data are available on request to the WEBT President, Massimo Villata (massimo.villata@inaf.it).

Code availability

The computer code used in this study is available in the Zenodo repository: https://zenodo.org/record/6562290#.YoVpVajMIuW; license: https://doi.org/10.5281/zenodo.6562290.

31. Villata, M. et al. The WEBT BL Lacertae campaign 2000. *Astron. Astrophys.* **390**, 407–421 (2002).
32. Raiteri, C. M. et al. WEBT multiwavelength monitoring and XMM-Newton observations of BL Lacertae in 2007–2008. Unveiling different emission components. *Astron. Astrophys.* **507**, 769–779 (2009).
33. Weaver, Z. R. et al. Multiwavelength variability of BL Lacertae measured with high time resolution. *Astrophys. J.* **900**, 137 (2020).
34. Fiorucci, M. & Tosti, G. VRI photometry of stars in the fields of 12 BL Lacertae objects. *Astron. Astrophys. Suppl. Ser.* **116**, 403–407 (1996).
35. Schmidt, G. D., Elston, R. & Lupie, O. L. The Hubble Space Telescope northern-hemisphere grid of stellar polarimetric standards. *Astron. J.* **104**, 1563–1567 (1992).
36. Nolan, P. L. et al. Fermi large area telescope second source catalog. *Astrophys. J. Suppl. Ser.* **199**, 31 (2012).
37. Alexander, T. in *Astronomical Time Series. Astrophysics and Space Science Library*, Vol. 218 (eds Maoz, D. Sternberg, A. & Leibowitz, E. M.) 163–170 (Springer, 1997).
38. Alexander, T. Improved AGN light curve analysis with the z-transformed discrete correlation function. Preprint at https://arxiv.org/abs/1302.1508 (2013).
39. Emmanoulopoulos, D., McHardy, I. M. & Papadakis, I. E. Generating artificial light curves: revisited and updated. *Mon. Not. R. Astron. Soc.* **433**, 907–927 (2013).
40. Done, C. et al. The X-ray variability of NGC 6814: power spectrum. *Astrophys. J.* **400**, 138–152 (1992).
41. Uttley, P., McHardy, I. M. & Papadakis, I. E. Measuring broad-band power spectra of active galactic nuclei with RXTE. *Mon. Not. R. Astron. Soc.* **332**, 231–250 (2005).
42. Chatterjee, R. et al. Correlated multi-wave band variability in the blazar 3C 279 from 1996 to 2007. *Astrophys. J.* **689**, 79 (2008).
43. Shepherd, M. C. Difmap: an interactive program for synthesis imaging. *ASP Conf. Ser.* **125**, 77–84 (1997).
44. Bach, U. et al. Structure and flux variability in the VLBI jet of BL Lacertae during the WEBT campaigns (1995–2004). *Astron. Astrophys.* **456**, 105–115 (2006).
45. Scargle, J. D. Studies in astronomical time series analysis. IV. Modeling chaotic and random processes with linear filters. *Astrophys. J.* **359**, 469–482 (1990).
46. Torrence, C. & Compo, G. P. A practical guide to wavelet analysis. *Bull. Am. Meteorol. Soc.* **79**, 61–78 (1998).
47. An, T. et al. Periodic radio variabilities in NRAO 530: a jet–disc connection? *Mon. Not. R. Astron. Soc.* **434**, 3487–3496 (2013).
48. O'Neill, S. et al. The unanticipated phenomenology of the blazar PKS 2131–021: a unique supermassive black hole binary candidate. *Astrophys. J. Lett.* **926**, L35 (2022).
49. Mizuno, Y. et al. Three-dimensional relativistic magnetohydrodynamic simulations of current-driven instability. I. Instability of a static column. *Astrophys. J.* **700**, 684 (2009).
50. Zhang, H. et al. Polarization signatures of kink instabilities in the blazar emission region from relativistic magnetohydrodynamic simulations. *Astrophys. J.* **835**, 125 (2017).
51. Bodo, G., Tavecchio, F. & Sironi, L. Kink-driven magnetic reconnection in relativistic jets: consequences for X-ray polarimetry of BL Lacs. *Mon. Not. R. Astron. Soc.* **501**, 2836–2847 (2021).
52. Acharya, S., Borse, N. S. & Vaidya, B. Numerical analysis of long-term variability of AGN jets through RMHD simulations. *Mon. Not. R. Astron. Soc.* **506**, 1862–1878 (2021).

Acknowledgements We dedicate this paper to Dr. Valeri M. Larionov, who was a prominent member of the WEBT collaboration. The research reported here is based on work supported in part by US National Science Foundation grants AST-2108622 and AST-2107806, and NASA Fermi GI grants 80NSSC20K1567, 80NSSC21K1917 and 80NSSC21K1951; by Shota Rustaveli National Science Foundation of Georgia under contract FR-19-6174; by the Bulgarian National Science Fund of the Ministry of Education and Science under grants DN 18-10/2017, DN 18-13/2017, KP-06-H28/3 (2018), KP-06-H38/4 (2019) and KP-06-KITAJ/2 (2020), and by National RI Roadmap Project D01-383/18.12.2020 of the Ministry of Education and Science of the Republic of Bulgaria; by JSPS KAKENHI grant #19K03930 of Japan; by the Ministry of Education, Science and Technological Development of the Republic of Serbia (contract 451-03-9/2021-14/200002) and observing grant support from the Institute of Astronomy and Rozhen NAO BAS through the bilateral joint research project 'Gaia Celestial Reference Frame (CRF) and fast variable astronomical objects'; by the Agenzia Spaziale Italiana (ASI) through contracts I/037/08/0, I/058/10/0, 2014-025-R.0, 2014-025-R.1.2015 and 2018-24-HH.0 to the Italian Istituto Nazionale di Astrofisica (INAF). H.Z. is supported by the NASA Postdoctoral Program at Goddard Space Flight Center, administered by ORAU. M.V.P. is partially supported by the Russian Foundation for Basic Research grant 20-02-00490. G.B. acknowledges support from the State Agency for Research of the Spanish MCIU through the 'Center of Excellence Severo Ochoa' award to the Instituto de Astrofísica de Andalucía (SEV-2017-0709) and from the Spanish 'Ministerio de Ciencia e Innovacíon' (MICINN) through grant PID2019-107847RB-C44. M.D.J. thanks the Brigham Young University Department of Physics and Astronomy for continued support of the extragalactic monitoring programme under way at the West Mountain Observatory. R.C. thanks ISRO for support under the AstroSat archival data utilization programme and BRNS for support through a project grant (sanction no. 57/14/10/2019-BRNS). The measurements at the Hans Haffner Observatory, Hettstadt, Germany, were supported by Baader Planetarium, Mammendorf, Germany. This study was based (in part) on observations conducted using the 1.8-m Perkins Telescope Observatory (PTO) in Arizona, USA, which is owned and operated by Boston University. These results made use of the Lowell Discovery Telescope (LDT) at Lowell Observatory. Lowell Observatory is a private, non-profit institution dedicated to astrophysical research and public appreciation of astronomy, and operates the LDT in partnership with Boston University, the University of Maryland and the University of Toledo. This paper is partly based on observations made with the IAC-80 operated on the island of Tenerife by the Instituto de Astrofisica de Canarias in the Spanish Observatorio del Teide and on observations made with the LCOGT telescopes, one of whose nodes is located at the Observatorios de Canarias del IAC on the island of Tenerife in the Observatorio del Teide. This paper is partly based on observations made with the Nordic Optical Telescope, owned in collaboration by the University of Turku and Aarhus University, and operated jointly by Aarhus University, the University of Turku and the University of Oslo, representing Denmark, Finland and Norway, the University of Iceland and Stockholm University at the Observatorio del Roque de los Muchachos, La Palma, Spain, of the Instituto de Astrofisica de Canarias. The VLBA is an instrument of the NRAO, USA. The NRAO is a facility of the National Science Foundation operated under cooperative agreement by Associated Universities, Inc.

Author contributions S.G.J.: developing and writing the paper, optical and VLBA observations and data reduction, periodicity analysis, data modelling; A.P.M.: VLBA observations and analysis, theoretical modelling, writing the paper; C.M.R. and M.V.: WEBT coordinators, optical data assembling, REDFIT analysis, writing the paper; Z.R.W.: optical observations and transformations, correlation analysis and simulation of light curves, WWZ analysis, VLBA image modelling, writing the paper; H.Z.: kink instability model development and application, theoretical model writing; L.D.: kink instability model development and application; J.L.G.: VLBA data imaging; M.V.P.: CWT analysis; S.S.S.: optical observations, γ-ray data reduction and description; V.M.L.: optical data reduction and WEBT data assembling; R.C.: power spectral response method analysis; V.M.L., D.C., W.P.C., O.M.K., A.M., K.Matsumoto and F.M.: leaders of observational groups that contributed more than 1,000 measurements to the optical datasets; the rest of the authors are members of the WEBT collaboration and have contributed to the paper by providing results of optical observations.

Competing interests The authors declare no competing interests.

Additional information

Supplementary information The online version contains supplementary material available at https://doi.org/10.1038/s41586-022-05038-9.

Correspondence and requests for materials should be addressed to S. G. Jorstad.

Peer review information *Nature* thanks Su Yao and the other, anonymous, reviewer(s) for their contribution to the peer review of this work. Peer reviewer reports are available.

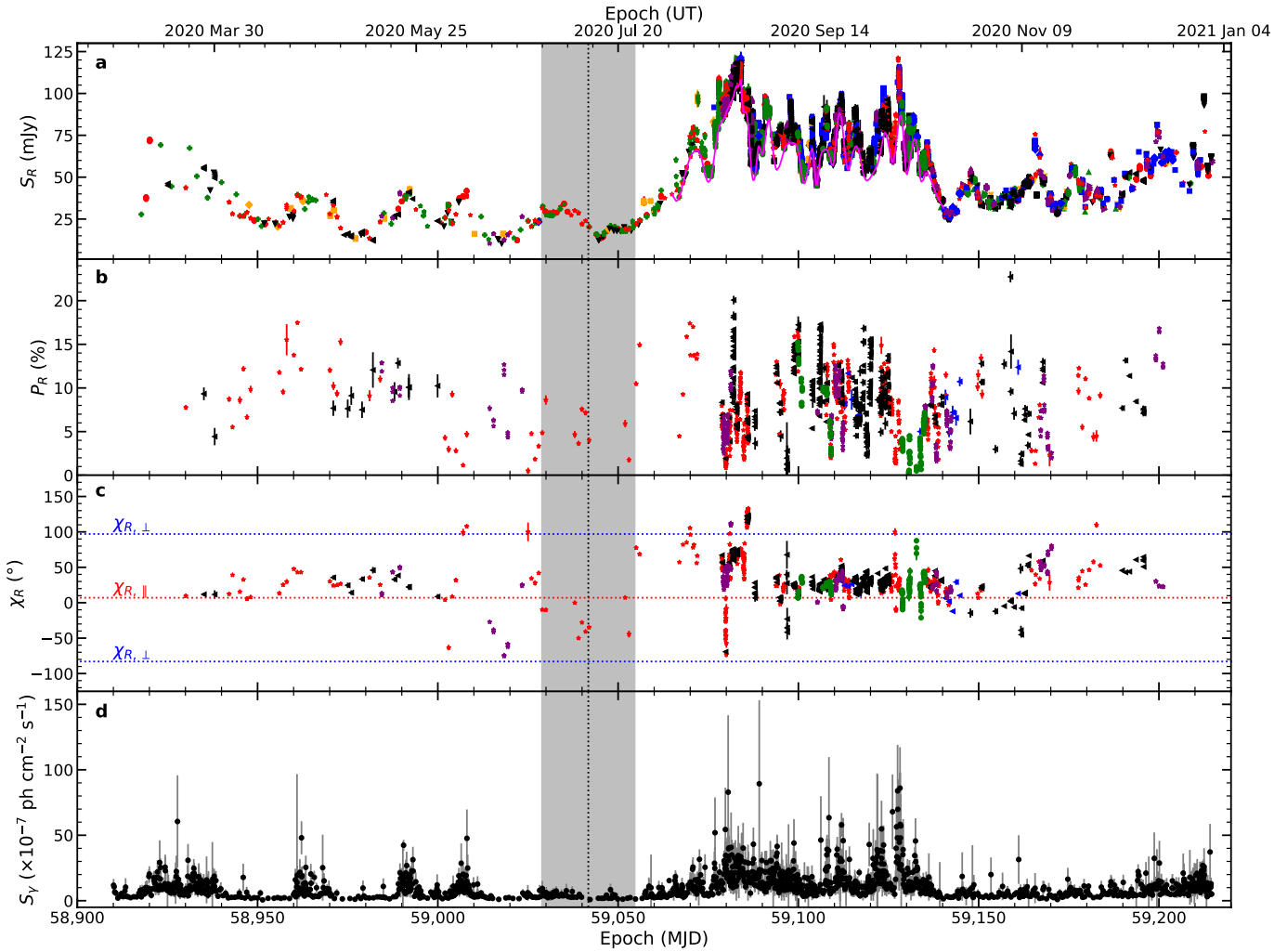

Extended Data Fig. 1 | BL Lac *R*-band optical and γ-ray data in 2020. **a**, *R*-band flux density light curve ($n = 16{,}497$). The solid magenta curve during the outburst plots a spline approximation of the long-term trend. **b**, Degree of polarization versus time ($n = 1{,}285$). **c**, Position angle of polarization versus time ($n = 1{,}285$). The red and blue dotted lines mark directions along and transverse to the jet axis, respectively. **d**, γ-Ray light curve ($n = 1{,}398$). The grey area denotes the 1σ uncertainty in the time of ejection of superluminal knot K (dotted grey line). Different symbols and colours indicate observations conducted by different telescopes, designations of which are given in Extended Data Table 1. The error bars are 1σ uncertainties (in plot **a**, they are smaller than the symbols).

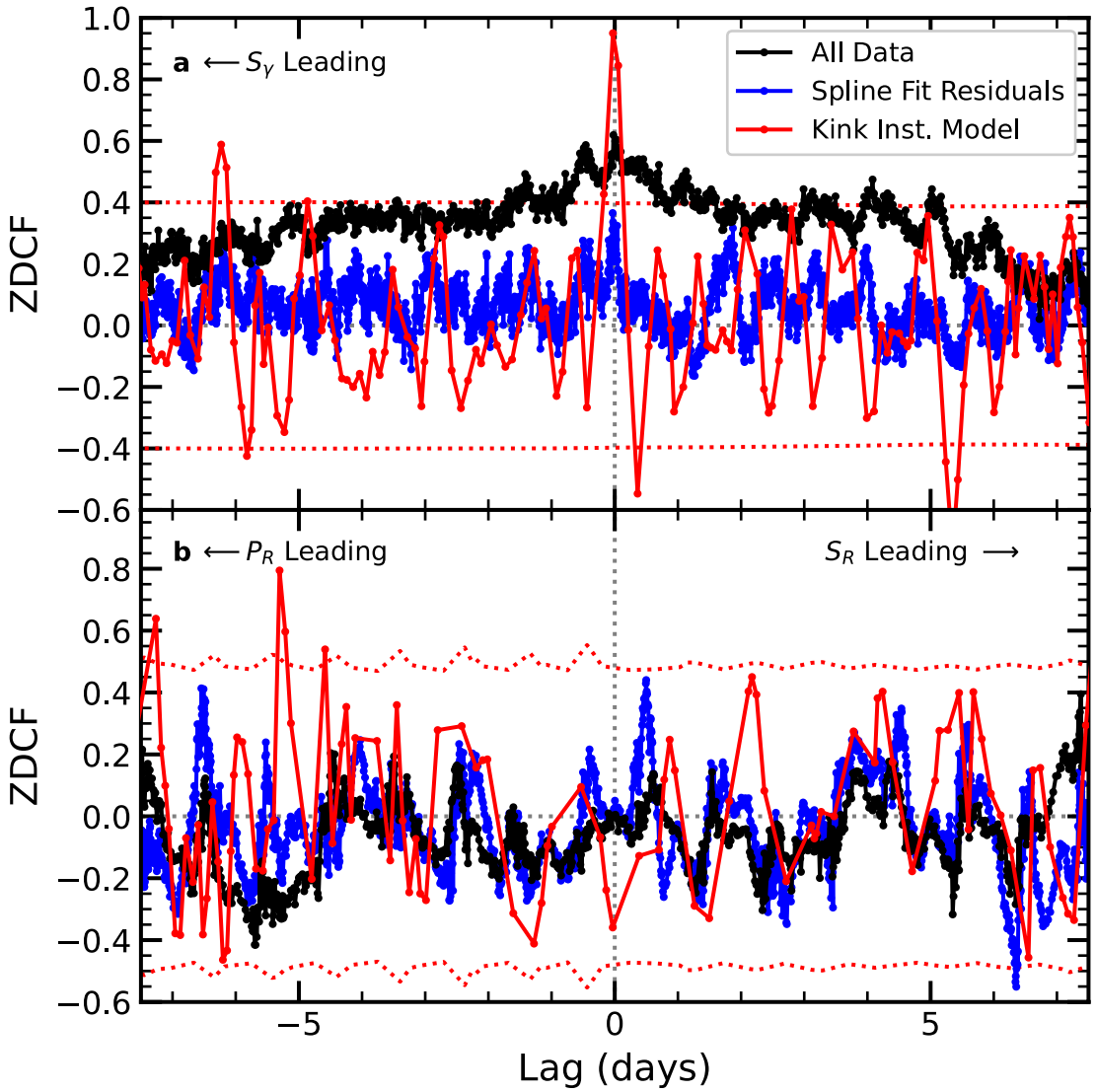

Extended Data Fig. 2 | Correlation analysis. a, *z*-Transformed discrete correlation function correlations between the γ-ray and *R*-band light curves for the entire dataset (black), between the γ-ray flux and *R*-band flux density residuals (blue) and between the theoretical γ-ray and *R*-band light curves (red) during the highest outburst state shown in Fig. 2. **b**, *z*-Transformed discrete correlation function correlations between the *R*-band flux density and degree of polarization for similar periods as in plot **a**. The dotted red horizontal lines correspond to 3σ probability of chance occurrence.

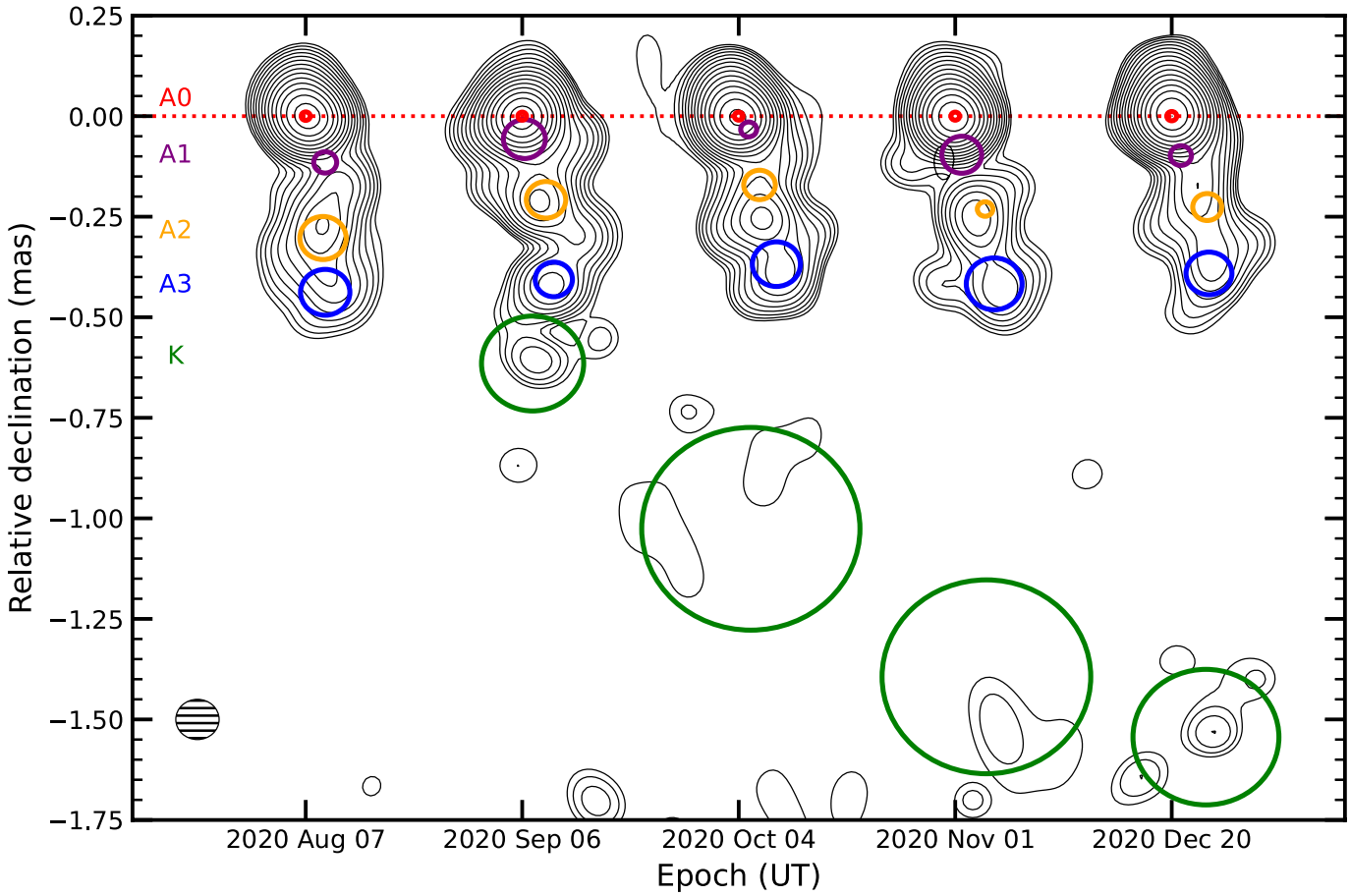

Extended Data Fig. 3 | VLBA total-intensity images of BL Lac at 43 GHz. The global intensity peak is 3.148 Jy beam^{-1} and contour levels start at 0.4% of the peak, then increase by factors of √2. Images are convolved with a circular beam of radius 0.1 mas (bottom-left circle). The coloured circles represent the FWHM areas of Gaussian components used to model the intensity distribution at each epoch, with colours matching those in Fig. 3b.

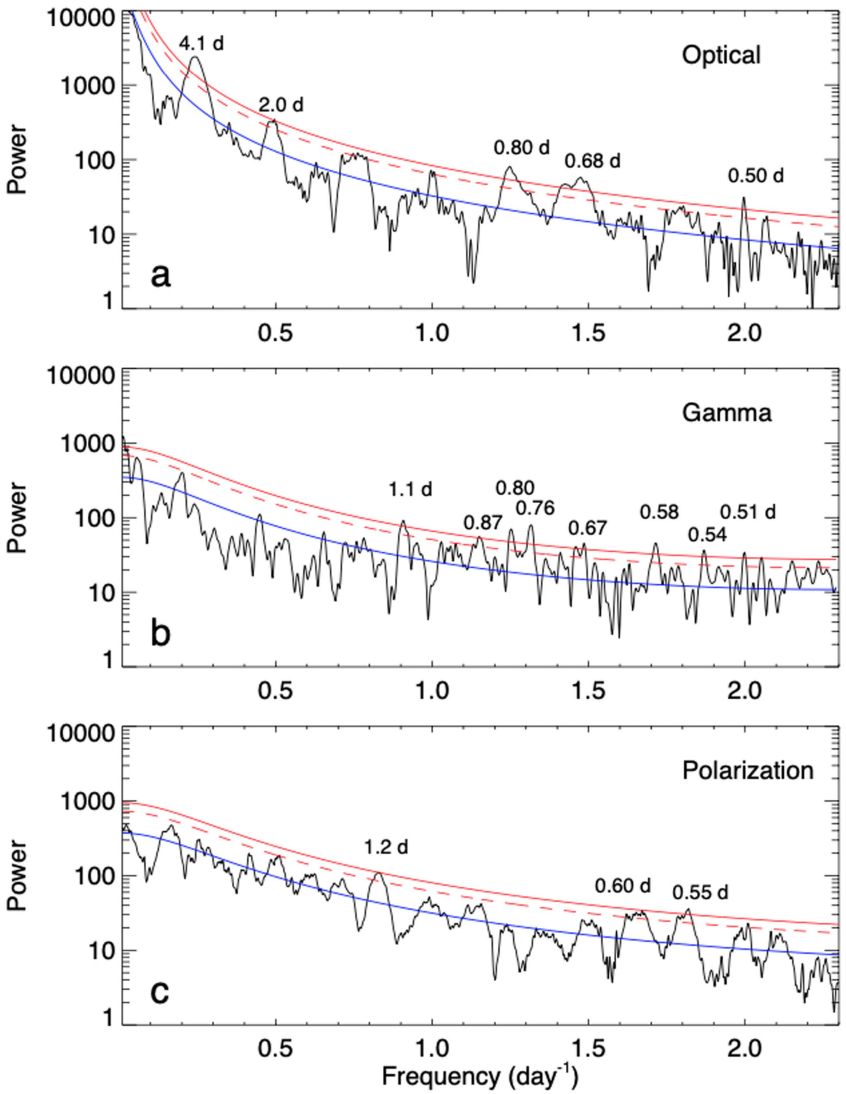

Extended Data Fig. 4 | REDFIT periodograms. a, For optical flux densities. **b**, For γ-ray fluxes. **c**, For degree of polarization. The black curves show the corrected periodograms; the blue lines represent the theoretical red-noise spectra; the red lines mark the 99% (solid) and 95% (dashed) significance levels. The periods corresponding to the most significant peaks, touching or exceeding the 99% levels, are indicated.

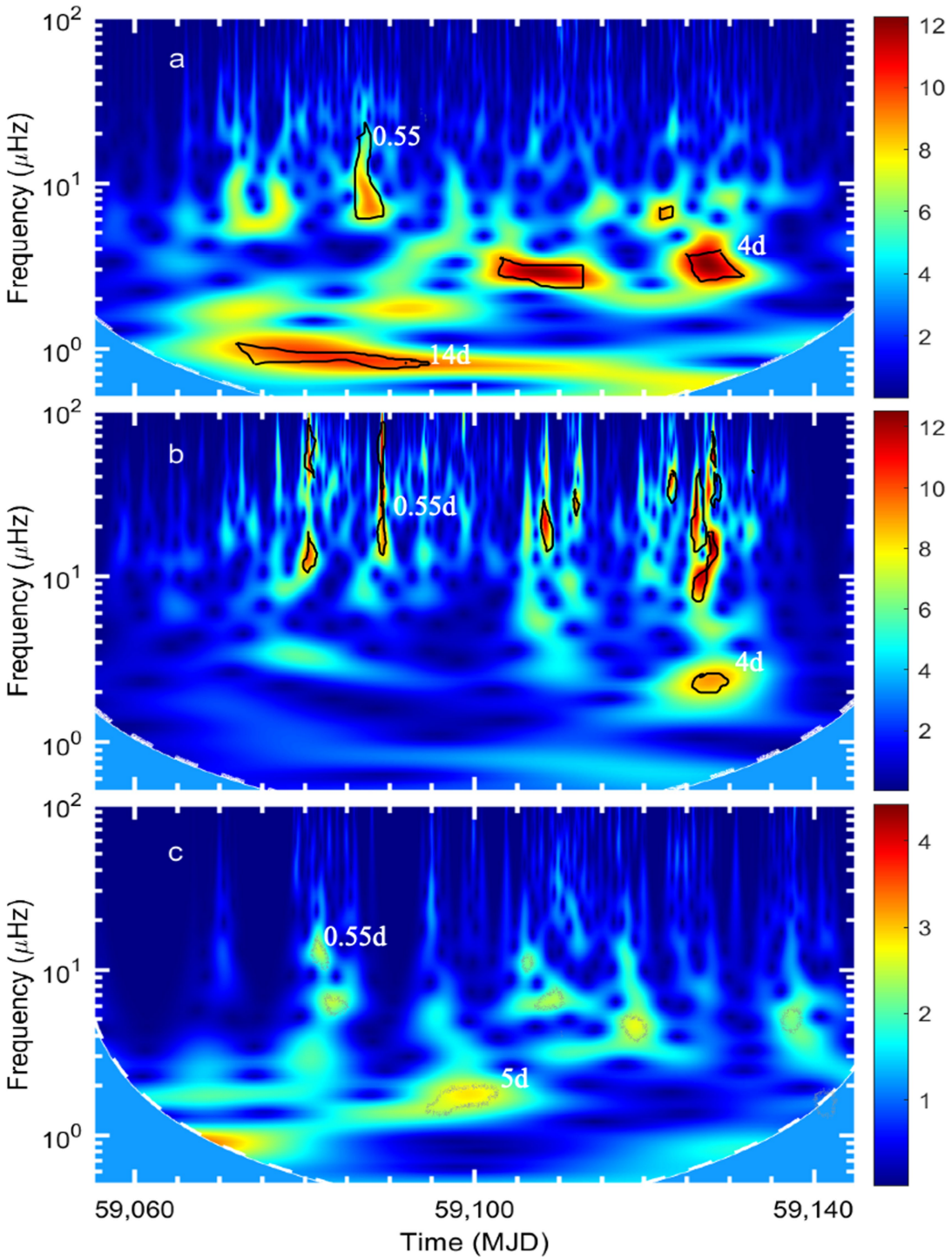

Extended Data Fig. 5 | CWT magnitude scalograms. For the *R*-band light curve (**a**), the γ-ray light curve (**b**) and the fractional polarization curve (**c**). Black contours in **a** and **b** indicate periods significant at the 99% level; grey contours in **c** indicate periods significant at the 92% level. Dashed white curves represent a cone of influence (COI), in which the information outside is affected by edge artefacts; numbers near contours indicate some periods for clarity.

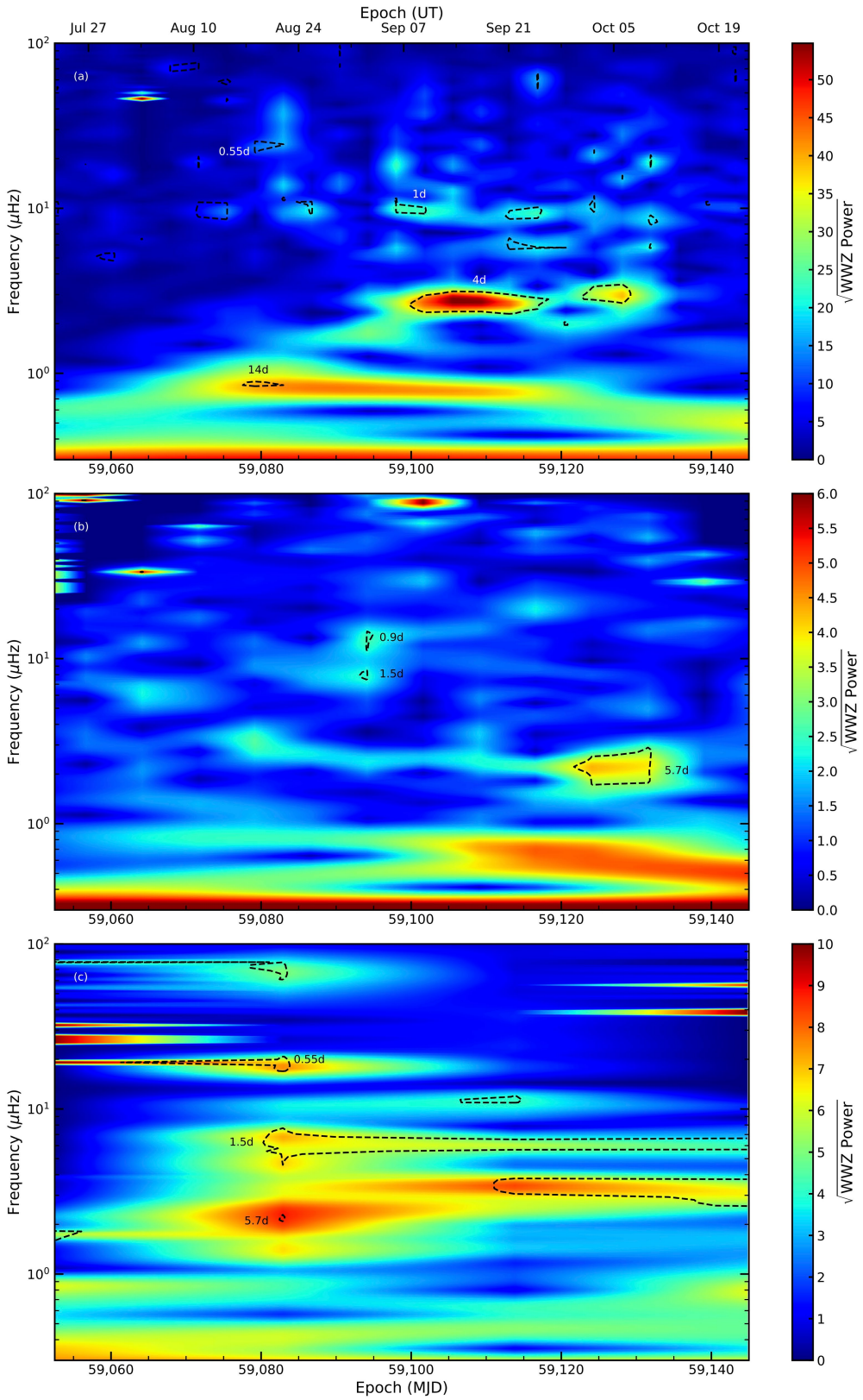

Extended Data Fig. 6 | WWZ transforms. For the *R*-band light curve (**a**), the γ-ray light curve (**b**) and the fractional polarization curve (**c**). Dashed black curves indicate periods significant at the 99% level; numbers near contours indicate some periods for clarity.

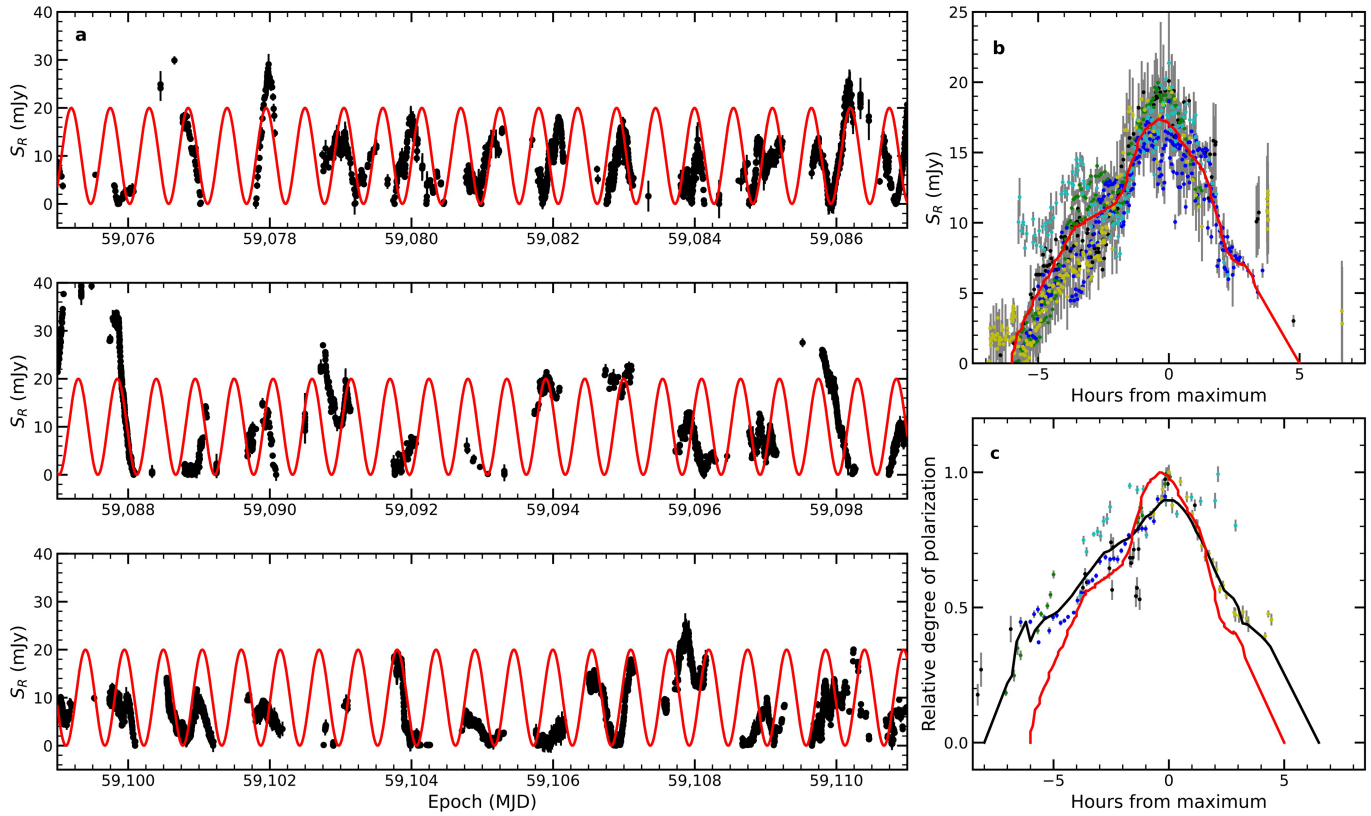

Extended Data Fig. 7 | QPOs in optical *R*-band flux density. a, Oscillations in optical *R*-band flux density during the outburst over the time interval 13 August 2020 to 18 September 2020 ($n = 8{,}106$), with the long-term trend subtracted. For comparison, the red curve represents a sinusoidal function with a period of 0.55 days and an amplitude of 20 mJy. **b**, Average profile of the optical flux density pulse (solid red curve). different colours indicate different pulses (2, 5, 7, 8, 9 and 12, as numbered in Fig. 1b). **c**, Average profile (solid black curve) of fractional polarization pulses (colour symbols), each normalized by its maximum, and normalized average profile of *R*-band flux density pulse (solid red curve). In all plots, error bars represent 1σ uncertainties.

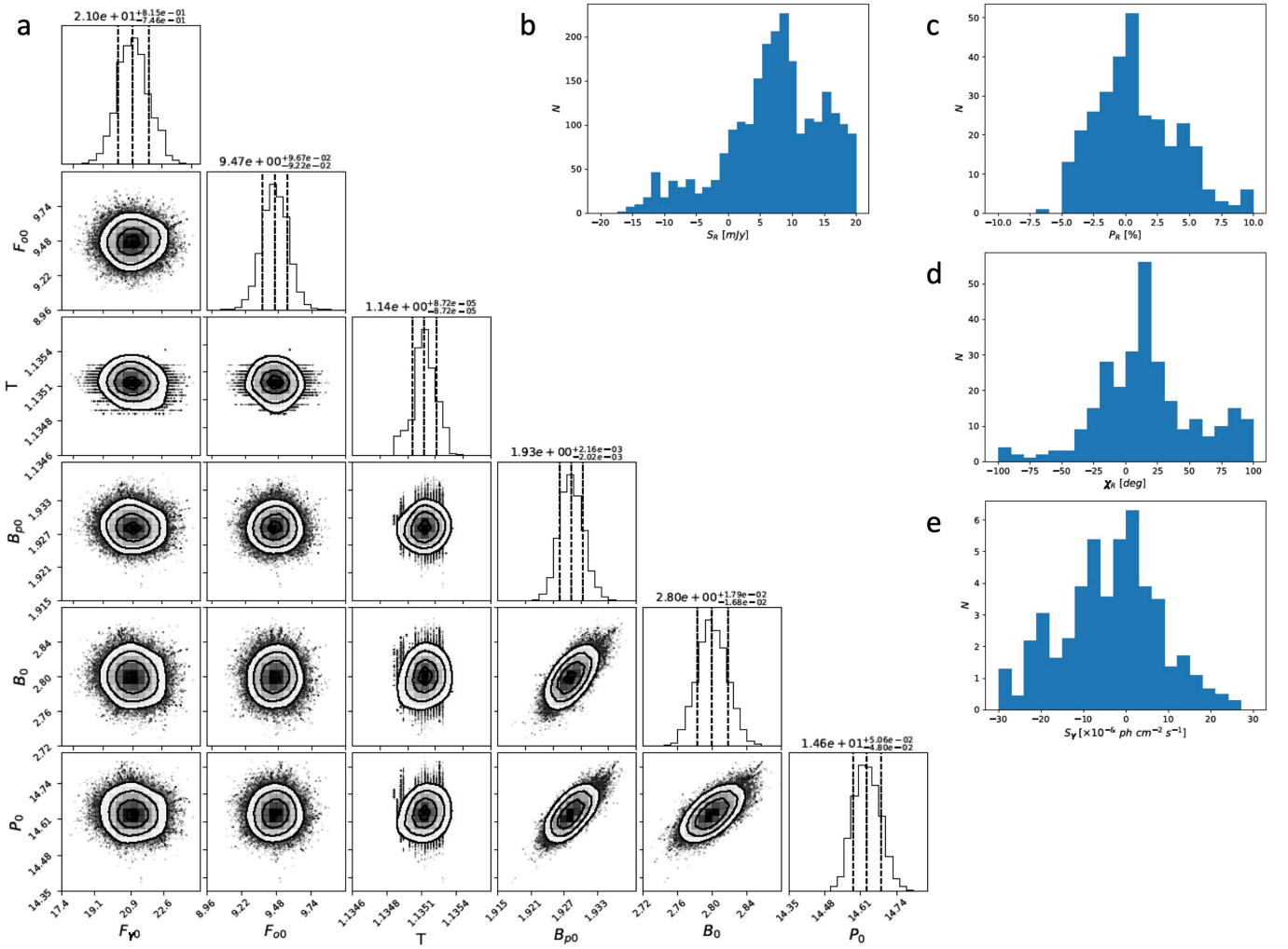

Extended Data Fig. 8 | MCMC model parameters. a, Triangle plot of posterior distributions of model parameters, sampled from 64 walkers with 60,000 iterations through MCMC; dashed lines in the histogram represent 16%, 50% and 84% quantiles, respectively (from left to right), for each parameter (see Methods). **b**–**e**, Distributions of residuals between the data and the model presented in Fig. 2 for *R*-band flux density (**b**), degree (**c**) and position angle (**d**) of polarization, and γ-ray flux (**e**).

Extended Data Table 1 | Optical telescopes

Observatory (Telescope; Camera)	Country	N_{obs}	$\langle\sigma_R\rangle$	Color	Symbol
Abastumani (70 cm)	Georgia	1631	0.008	Red	●
Aoyama Gakuin (35 cm)	Japan	32	0.022	Orange	▼
ARIES (104 cm)	India	2	0.005	Green	▲
ARIES (130 cm)	India	15	0.005	Green	▲
Belogradchik (60 cm; pol)	Bulgaria	28	0.028	Blue	◀
Catania (Arena; 20 cm)	Italy	134	0.008	Purple	▶
Catania (GAC; 25 cm)	Italy	151	0.009	Purple	▶
Catania (SLN; 91 cm)	Italy	230	0.005	Purple	▶
Connecticut (51 cm)	USA	181	0.020	Black	■
Crimean (AP7p; 70 cm)	Crimea	137	0.007	Red	★
Crimean (ST-7; 70 cm; pol)	Crimea	892	0.007	Red	★
Crimean (ST-7; 70 cm)	Crimea	12	0.010	Red	★
Haleakala (LCO; 40 cm)	USA	14	0.046	Orange	♦
Hans Haffner (50 cm)	Germany	591	0.005	Green	✚
Hypatia (25 cm)	Italy	4164	0.005	Blue	✖
Lowell (LDT; 430 cm)	USA	7	0.013	Purple	●
Lulin (SLT; 40 cm)	Taiwan	1014	0.012	Black	▼
McDonald (LCO; 40 cm)	USA	13	0.044	Red	▲
Montarrenti (53 cm)	Italy	9	0.006	Orange	◀
Mt. Maidanak (T-60; FLI; 60 cm)	Uzbekistan	240	0.011	Green	▶
Osaka Kyoiku (51 cm)	Japan	1610	0.007	Blue	■
Perkins (180 cm; pol)	USA	293	0.005	Purple	★
Pulkovo (65 cm)	Russia	23	0.015	Black	♦
Roque (NOT; e2v; 256 cm)	Spain	15	0.024	Red	✚
Rozhen (200 cm)	Bulgaria	72	0.025	Orange	✖
Rozhen (50/70 cm)	Bulgaria	99	0.027	Orange	✖
SAI (FLI; Zeiss-600; 60 cm)	Crimea	455	0.009	Green	●
SAI (ZTSH; 260 cm; pol)**	Crimea	141	0.009	Green	●
Seveso (30 cm)	Italy	183	0.010	Blue	▼
Siena (30 cm)	Italy	1056	0.005	Purple	▲
St. Petersburg (40 cm; pol)	Russia	767	0.010	Black	◀
Svetloe (40 cm)	Russia	5	0.029	Red	▶
Teide (IAC80; 80 cm)	Spain	30	0.040	Orange	■
Teide (LCO; 40 cm)	Spain	11	0.050	Orange	■
Tijarafe (40 cm)	Spain	1314	0.029	Green	★
Vidojevica (140 cm)	Serbia	97	0.006	Blue	♦
Vidojevica (60 cm)	Serbia	116	0.011	Blue	♦
West Mountain (90 cm)	USA	222	0.005	Purple	✚
Wild Boar (24 cm)	Italy	632	0.005	Black	✖

Columns are: 1, telescope, the telescopes marked 'pol' provided polarization observations along with photometric data, except ZTSH, marked **, which provided only polarization data; 2, country of the observatory; 3, number of *R*-band measurements used in Extended Data Fig. 1a; 4, average 1σ uncertainty of a measurement; 5 and 6, colour and symbol, respectively, designated to each telescope.